18th AIAA/CEAS Aeroacoustics Conference (33rd AIAA Aeroacoustics Conference)
04 - 06 June 2012, Colorado Springs, CO

AIAA 2012-2163

Statistical Modeling of BBSAN Including Refraction Effects

Cyprien Henry*
Snecma, Safran Group, 77550 Moissy-Cramayel, France

Christophe Bailly†
Laboratoire de Mecanique des Fluides et d'Acoustique
UMR CNRS 5509, Ecole Centrale de Lyon 69134 Ecully, France

Guillaume Bodard‡
Snecma, Safran Group, 77550 Moissy-Cramayel, France

When operated at off-design conditions, supersonic jets produce BroadBand Shock-Associated Noise (BBSAN). This noise is generated by the interaction of the quasi-periodic shock-cell structure with the large scale turbulence. BBSAN radiation is characterized by multiple frequency humps dominating the jet turbulent mixing noise in the forward quadrant. A semi-analytical prediction method is presented in this paper. BBSAN sources are formally derived from the Linearized Euler Equations and then numerically computed from a calculation of the turbulent mean flow. Moreover, a ray-tracing method is used to account for refraction effects. Predicted acoustic results are compared with experimental data to assess the model capabilities.

Nomenclature

c	Speed of sound
D	Nozzle exit diameter
f_p	Peak frequency of BBSAN
g_L	Green's function of Lilley's equation
l	Characteristic length scale in the streamwise direction
$l_\perp$	Characteristic length scale in the cross-stream direction
M_d	Nozzle design Mach number
M_j	Isentropic jet Mach number
NPR	Nozzle pressure ratio p_t/p_∞
p	Static pressure
p_t	Stagnation pressure
PSD	Power Spectrum Density
R_{pp}	Cross spectral density
SPL	Sound Pressure Level
St	Strouhal number
S_{pp}	Power spectral density
u_c	Convection velocity
u_j	Isentropic jet velocity
v_i	Velocity component in the i-direction
$\boldsymbol{x} = (x_i)_{i=1,2,3}$	Observer location

Greek letters

*PhD Student, Acoustics Department, cyprien.henry@gmail.com
†Professor at Ecole Centrale de Lyon, Senior AIAA Member, christophe.bailly@ec-lyon.fr
‡PhD Engineer, Acoustics Department, guillaume.bodard@snecma.fr

$\boldsymbol{\eta} = (\xi, \gamma, \zeta)$	Vector joining two point sources
Φ	Inlet angle
γ	Specific heat ratio of air
ω	Angular frequency
π	Non dimensional pressure
Π_n	Vector Green's functions
ρ	Air density

Subscripts

i	Variable number
s	Shock induced perturbations
t	Turbulence induced perturbations
τ_s	Turbulence characteristic time scale
∞	Undisturbed quantities

Superscripts

$'$	Acoustic perturbations
$*$	Complex conjugate

I. Introduction

When a supersonic jet is operated at off design conditions, the static pressure in the jet at the nozzle exit does not match the ambient pressure. As a result, a series of expansion fans and compression cells appears, the role of which is to bring the static pressure in the jet plume to the ambient pressure. If the static pressure at the nozzle exit is higher than the ambient pressure, the shocked jet is said to be underexpanded. Otherwise, it is overexpanded. Only underexpanded jets are considered in this paper.

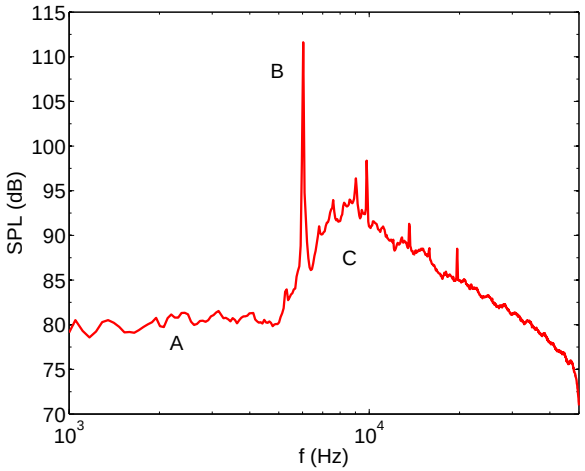

Figure 1. Far-field sound pressure levels of a supersonic shocked jet. $M_j = 1.15$, $\theta = 130^\circ$ **(downstream reference),** $R/D = 53.2$. **A: mixing noise, B: screech, C: BBSAN. Measurements by André et al.**[1]

Both subsonic and supersonic jets produce turbulent mixing noise. This noise originates from the turbulence developing in the mixing layer between the jet flow and the ambient medium. This broadband noise is shown in Figure 1 (part A of the spectrum) in which a typical spectrum of a shocked jet is presented. Shocked jets contain two additional sources of noise, as compared to perfectly expanded jets. Screech is the first one. Powell assumed that a feedback loop between shocks and the nozzle lip was responsible for screech. Berland et al.[2] studied this phenomenon numerically, for the case of an underexpanded planar jet. Screech tones produce a sharp peak on the Sound Pressure Levels (SPLs), as shown in Figure 1 (part B of the spectrum). The second additional source of noise is BroadBand Shock-Associated Noise (BBSAN). It

is the subject of this paper. Physically, BBSAN is created by the interaction of the jet shock-cell pattern with the turbulence from the mixing layer. BBSAN is a wide frequency range phenomenon that dominates mixing noise in the upstream direction. It corresponds to part C of Figure 1. Harper-Bourne and Fisher[3] were the first to thoroughly study BBSAN. They exhibited the key role of the parameter $\beta = \sqrt{M_j^2 - 1}$ to propose dimensional laws. The isentropic jet Mach number M_j depends only on the Nozzle Pressure Ratio (NPR), that is the ratio of the stagnation pressure in the jet p_t to the ambient pressure p_∞

$$\mathrm{NPR} = \frac{p_t}{p_\infty} = \left[1 + \frac{\gamma - 1}{2} M_j^2\right]^{\gamma/(\gamma-1)} \tag{1}$$

They observed from experiments that BBSAN intensity follows a β^4 law, and noticed that the pressure jump across a normal shock (i.e. the shock strength) depends on β^2. Their fundamental conclusion is that the strength of BBSAN sources scales like the shock strength in the jet. Furthermore, BBSAN overwhelms mixing noise in the upstream direction and seems omnidirectional in this region. Lastly, the interaction between the shock-cell structure and the turbulent eddies from the mixing layer is the physical mechanism for BBSAN. These conclusions led Harper-Bourne and Fisher to the following semi-empirical model for BBSAN radiation: BBSAN is modeled by a linear distribution of monopole sources, located at the end of each shock-cell. The monopoles are correlated and the phase is determined by the eddy convection velocity. Such a model relates the characteristic peak frequency f_p of BBSAN to the mean shock-cell length L

$$f_p = \frac{u_c}{L(1 - M_c \cos\theta)} \tag{2}$$

where u_c is the eddy convection speed, $M_c = u_c/c_\infty$ is the convection Mach number and θ is the angle of observation (downstream reference). According to (2), f_p increases when the observer moves from the upstream to the downstream direction, which is confirmed by experiments. Harper Bourne and Fisher's model is limited to far field predictions and relies neither on the nozzle geometry nor on the details of the turbulent flow field.

Tam predicted BBSAN using a different approach.[4,5] The pressure perturbation p_s created by the shock-cell pattern is calculated using a waveguide model, while large scale turbulence is described by instability waves traveling downstream. The weak interaction of these two phenomena creates BBSAN. Tam's model produces spectra in good agreement with experiments. It has been extended to dual-stream jets,[6] but in this case, only the peak frequency is available.

Those two models share the common limitation that they do not rely on the true flow field. A similar issue exists for mixing noise models. Bailly et al.[7,8] and Morris & Farassat,[9] among others, showed it was possible to feed the acoustic model with a turbulent mean flow calculation. A similar approach was recently used by Morris and Miller[10–12] for the prediction of BBSAN. The model is based on an acoustic analogy, and the Power Spectrum Density is expressed as a function of flow variables. As a result, the model can tackle complex geometry and even includes flight effect[13] using an adjoint approach. Morris and Miller's model is used as a starting point for the present work.

The paper is organized as follows. The model development is detailed in the first part. At this stage, the source terms are propagated to the far field using the free field Green's function: the refraction effects due to the mean flow surrounding the shocked jets are neglected. Then, results on single-stream jets are shown. The next part tackles the inclusion of refraction effects using ray-tracing to compute the Green's functions of the problem.

II. Model development

II.A. Physical model

The model relies on the LEE (Linearized Euler Equations). A dimensionless pressure variable π is introduced[14]

$$\pi = \frac{1}{\gamma} \ln\left(\frac{p}{p_\infty}\right) \tag{3}$$

where p is the static pressure and γ is the specific heat ratio of air. For air considered as a perfect gas, the relation $p = p(\rho, s)$ defines an equation of state, where s is the entropy and ρ the density. The total

derivative of p is

$$dp = \frac{\partial p}{\partial \rho}\Big|_s d\rho + \frac{\partial p}{\partial s}\Big|_\rho ds \quad \text{i.e.} \quad dp = c^2 d\rho + \frac{p}{c_v} ds \tag{4}$$

where c denotes the speed of sound and c_v the specific heat capacity at constant volume. The sound velocity is given by $c^2 = \gamma p/\rho$ so that

$$\frac{dp}{p} - \gamma \frac{d\rho}{\rho} = \frac{1}{c_v} ds \tag{5}$$

The conservation of mass can thus be written as,

$$\frac{\partial v_i}{\partial x_i} = -\frac{1}{\rho}\frac{D\rho}{Dt} = \frac{1}{\gamma}\left(\frac{1}{c_v}\frac{Ds}{Dt} - \frac{1}{p}\frac{Dp}{Dt}\right) \tag{6}$$

where D/Dt is the material derivative. Einstein notation is used. The flow is assumed to be isentropic, i.e. $Ds/Dt = 0$, which leads to

$$\frac{\partial v_i}{\partial x_i} = -\frac{1}{\gamma p}\frac{Dp}{Dt} = -\frac{1}{\gamma}\frac{D}{Dt}\left[\ln\left(\frac{p}{p_\infty}\right)\right] \tag{7}$$

Making use of π, the conservation of mass takes the following form,

$$\frac{D\pi}{Dt} + \frac{\partial v_i}{\partial x_i} = 0 \tag{8}$$

In the same way, the conservation of momentum can be arranged as

$$\frac{Dv_i}{Dt} + c^2 \frac{\partial \pi}{\partial x_i} = 0 \tag{9}$$

where v_i is the velocity component in the i-direction. To linearize (8) and (9), the flow field is split up among four contributions, as proposed by Lele[15] or Tam[5]

$$\begin{Bmatrix} \pi \\ v_i \end{Bmatrix} = \begin{Bmatrix} \bar{\pi} + \varepsilon_s \pi_s + \varepsilon_t \pi_t + \varepsilon_s \varepsilon_t \pi' \\ \bar{v}_i + \varepsilon_s v_{si} + \varepsilon_t v_{ti} + \varepsilon_s \varepsilon_t v' \end{Bmatrix} \tag{10}$$

where the overline denotes an average term, the subscripts s and t represents the perturbations due to the shock-cells and turbulence respectively, and the superscript $'$ accounts for the interaction between shock and turbulence, containing acoustic perturbations. ε_s and ε_t are two dimensionless parameters used to quantify the orders of magnitude of each perturbation. When inserting (10) into (8) and (9), only the terms of order $\varepsilon_s \varepsilon_t$ are kept. Indeed, the physical mechanism generating BBSAN is the interaction between shock-cells and turbulence, which makes this approximation consistent. Especially, interaction of turbulence with itself (ε_t^2 terms) is neglected: it represents mixing noise, which is much weaker than shock-cell noise for the considered problem. The shock-cell structure is assumed to be fixed with time and thus satisfies the steady version of (7)-(9). Taking this into account, the unsteady linearized system is

$$\begin{aligned} \frac{\partial \pi'}{\partial t} + \bar{v}_j \frac{\partial \pi'}{\partial x_j} + \frac{\partial v_i'}{\partial x_i} &= \theta \\ \frac{\partial v_i'}{\partial t} + \bar{v}_j \frac{\partial v_i'}{\partial x_j} + v_j' \frac{\partial \bar{v}_i}{\partial x_j} + \bar{c}^2 \frac{\partial \pi'}{\partial x_i} &= f_i^v + f_i^a \qquad i = 1,2,3 \end{aligned} \tag{11}$$

An interpretation of (11) is that a linear propagation operator is applied to the acoustic field, and source terms appear on the right-hand side, namely

$$\begin{aligned} \theta &= -v_{sj}\frac{\partial \pi_t}{\partial x_j} - v_{tj}\frac{\partial \pi_s}{\partial x_j} \\ f_i^v &= -v_{sj}\frac{\partial v_{ti}}{\partial x_j} - v_{tj}\frac{\partial v_{si}}{\partial x_j} \\ f_i^a &= -c_s^2\frac{\partial \pi_t}{\partial x_i} - c_t^2\frac{\partial \pi_s}{\partial x_i} \end{aligned} \tag{12}$$

Only f_i^v is of interest in the present study dealing with BBSAN. This term accounts for the interaction of the velocity perturbations due to shock-cells and turbulence. Consequently, f_i^a and θ are now neglected in what follows. The simplified system to be solved is given by,

$$\frac{\partial \pi'}{\partial t} + \overline{v_j}\frac{\partial \pi'}{\partial x_j} + \frac{\partial v_i'}{\partial x_i} = 0 \tag{13a}$$

$$\frac{\partial v_i'}{\partial t} + \overline{v_j}\frac{\partial v_i'}{\partial x_j} + v_j'\frac{\partial \overline{v_i}}{\partial x_j} + \overline{c}^2\frac{\partial \pi'}{\partial x_i} = f_i \tag{13b}$$

II.B. Calculation of the associated Green's functions

Since (13a)-(13b) is a linear differential system, the Green's function technique is well suited. According to Duffy,[16] one has to find a set of functions $\{\Pi_n, V_{ni},\ 0 \leq n \leq 3\}$ satisfying

$$\frac{\partial \Pi_n}{\partial t} + \overline{v}_j\frac{\partial \Pi_n}{\partial x_j} + \frac{\partial V_{ni}}{\partial x_i} = \delta(\boldsymbol{x}-\boldsymbol{y})\delta(t-t_1)\delta_{0n} \tag{14a}$$

$$\frac{\partial V_{ni}}{\partial t} + \overline{v}_j\frac{\partial V_{ni}}{\partial x_j} + V_{nj}\frac{\partial \overline{v}_i}{\partial x_j} + \overline{c}^2\frac{\partial \Pi_n}{\partial x_i} = \delta(\boldsymbol{x}-\boldsymbol{y})\delta(t-t_1)\delta_{in} \tag{14b}$$

where δ is the Dirac distribution and δ_{in} is the Kronecker delta. Since there is no source term in (13a), $\Pi_0 = 0$ and $V_{0i} = 0$ for $1 \leq i \leq 3$. The acoustic pressure π' is directly related to the source terms through the following integral

$$\pi'(\boldsymbol{x},t) = \iint \Pi_n(\boldsymbol{x},\boldsymbol{y},t-t_1) f_n(\boldsymbol{y},t_1) d\boldsymbol{y} dt_1 \tag{15}$$

Once again, the summation over the three components f_n of the source term is implied here.

The Green's functions in the absence of a mean flow will now be derived. Physically, refraction due to the jet shear layer or any external flow surrounding the shocked jet is neglected. The validity of this approximation is discussed further in section IV. The speed of sound is constant in this specific case and $\overline{c} = c_\infty$. Mathematically, the mean velocity components are set to $\overline{v}_j = 0$ in (13a)-(13b), which yields

$$\frac{\partial \pi'}{\partial t} + \frac{\partial v_i'}{\partial x_i} = 0 \tag{16a}$$

$$\frac{\partial v_i'}{\partial t} + c_\infty^2\frac{\partial \pi'}{\partial x_i} = f_i \tag{16b}$$

System (16) describes the propagation of an acoustic perturbation due to a source term f_i in a quiescent medium. The medium being at rest, the velocity fluctuations may be classically eliminated by combining (16a) and (16b)

$$\frac{\partial}{\partial t}(16a) - \frac{\partial}{\partial x_i}(16b) = \frac{\partial^2 \pi'}{\partial t^2} - c_\infty^2 \Delta \pi' = -\nabla \cdot \boldsymbol{f} \tag{17}$$

to form the well-known wave equation, where $-\nabla \cdot \boldsymbol{f}$ is a force source term. What is shown here, is that the pressure perturbation π' satisfies a set of ordinary differential equations (the LEE) as well as a wave equation. The free field Green's function $g_\infty(\boldsymbol{x},t|\boldsymbol{y},t_1)$ associated with the wave equation satisfies

$$\frac{\partial^2 g_\infty}{\partial t^2} - c_\infty^2 \Delta g_\infty = \delta(\boldsymbol{x}-\boldsymbol{y})\delta(t-t_1) \tag{18}$$

This is the response of the medium at location $\boldsymbol{x}$ and time t for a pulse emitted at location $\boldsymbol{y}$ and time t_1. This function is given by[16]

$$g_\infty(\boldsymbol{x},t|\boldsymbol{y},t_1) = \frac{\delta(t-t_1-|\boldsymbol{x}-\boldsymbol{y}|/c_\infty)}{4\pi|\boldsymbol{x}-\boldsymbol{y}|c_\infty^2} \tag{19}$$

and the formal solution to (18) is

$$\pi'(\boldsymbol{x},t) = -\int g(\boldsymbol{x},\boldsymbol{y},t-t_1)\nabla \cdot \boldsymbol{f}(\boldsymbol{y},t_1) d\boldsymbol{y} dt_1 \tag{20}$$

Using properties of the convolution product, the divergence operator may be applied to the Green's function,

$$\pi'(\boldsymbol{x},t) = \iint \left(\frac{\partial g_\infty}{\partial y_n}(\boldsymbol{x},\boldsymbol{y},t-t_1) \right) f_n(\boldsymbol{y},t_1) d\boldsymbol{y} dt_1 \tag{21}$$

Direct identification between (15) and (21) provides

$$\Pi_n(\boldsymbol{x},\boldsymbol{y},t-t_1) = \frac{\partial g_\infty}{\partial y_n}(\boldsymbol{x},\boldsymbol{y},t-t_1) \tag{22}$$

This equation relates the vector Green's functions Π_n of the LEE to the free field Green's function g_∞ of the wave equation. The next calculations will be performed in the frequency domain. The following convention is used for the Fourier transform

$$h(\omega) = \int_{-\infty}^{+\infty} h(t) e^{-i\omega t} dt \qquad h(t) = \frac{1}{2\pi} \int_{-\infty}^{+\infty} h(\omega) e^{i\omega t} d\omega \tag{23}$$

In the frequency domain, the vector Green's functions are given by

$$\Pi_n(\boldsymbol{x},\boldsymbol{y},\omega) = \frac{\partial g_\infty}{\partial y_n}(\boldsymbol{x},\boldsymbol{y},\omega) \tag{24}$$

The free field Green's function in the frequency domain is straightforwardly computed

$$g_\infty(\boldsymbol{x},\boldsymbol{y},\omega) = \frac{e^{-i\omega \frac{|\boldsymbol{x}-\boldsymbol{y}|}{c_\infty}}}{4\pi c_\infty^2 |\boldsymbol{x}-\boldsymbol{y}|} \tag{25}$$

After some algebra, one finds the Green's functions associated with the initial LEE system

$$\Pi_n(\boldsymbol{x},\boldsymbol{y},\omega) = \frac{e^{-i\omega|\boldsymbol{x}-\boldsymbol{y}|/c_\infty}}{4\pi c_\infty^2} \frac{i\omega}{c_\infty} \frac{x_n}{|\boldsymbol{x}|^2} \tag{26}$$

This expression relies on a far field approximation. First, the observation distance $|\boldsymbol{x}|$ is much larger than the size of the source domain $|\boldsymbol{y}|$, that is $|\boldsymbol{y}|/|\boldsymbol{x}| << 1$, corresponding to the geometric far field assumption. Second, the observation distance is much larger than the characteristic wavelength. For a nozzle diameter $D = 0.038$m at a jet Mach number $M_j = 1.15$, the lowest frequency of interest is around $f = 1000$Hz, which corresponds to a wavelength $\lambda = c/f \approx 10$D. Typical distances of observation range from 50D to 100D so that the acoustic far field condition is clearly met

Now that π' is known, π is asymptotically expanded assuming small perturbations

$$\pi = \frac{1}{\gamma} \ln \left(\frac{\overline{p} + p_s + p_t + p'}{p_\infty} \right) = \overline{\pi} + \frac{1}{\gamma} \left(\frac{p_s}{p_\infty} + \frac{p_t}{p_\infty} + \frac{p'}{p_\infty} \right) \tag{27}$$

Comparing (27) with the original expression of π leads to the approximation $p' = \gamma p_\infty \pi'$ and recalling that $c_\infty^2 = \gamma p_\infty / \rho_\infty$ gives $p' = \rho_\infty c_\infty^2 \pi'$. The final expression for the acoustic pressure as a function of the Green's functions and the source terms is

$$p'(\boldsymbol{x},t) = \rho_\infty c_\infty^2 \iint \Pi_n(\boldsymbol{x},\boldsymbol{y},t-t_1) f_n(\boldsymbol{y},t_1) \, d\boldsymbol{y} \, dt_1 \tag{28}$$

II.C. Estimation of the pressure correlation function

In this section, the pressure correlation function R_{pp} is formally derived. The pressure signal is treated as a random, time-dependent, signal. Physically, N acoustic pressure measurements will give N different spectra but the signal is assumed to be stationary, i.e. its statistical properties are constant over time. Mathematically it is a stochastic process, the k^{th} realization of which is

$$p^{(k)}(\boldsymbol{x},t) = \rho_\infty c_\infty^2 \iint \Pi_n(\boldsymbol{x},\boldsymbol{y},t-t_1) f_n^{(k)}(\boldsymbol{y},t_1) \, d\boldsymbol{y} \, dt_1 \tag{29}$$

The randomness of the signal is due to the source terms, not to the Green's functions that are deterministic. It is more convenient to make use of the spectral Green's functions in (29), so that the acoustic pressure is given by

$$p^{(k)}(\boldsymbol{x},t) = \frac{\rho_\infty c_\infty^2}{2\pi} \iiint \Pi_n(\boldsymbol{x},\boldsymbol{y},\omega) f_n^{(k)}(\boldsymbol{y},t_1) e^{i\omega(t-t_1)} d\omega d\boldsymbol{y} dt_1 \tag{30}$$

The pressure correlation function over time is the ensemble average

$$\begin{aligned} R_{pp}(\boldsymbol{x},\tau) &= < p^{(k)}(\boldsymbol{x},t) p^{*(k)}(\boldsymbol{x},t+\tau) > \\ R_{pp}(\boldsymbol{x},\tau) &= \lim_{N\to+\infty} \frac{1}{N} \sum_{k=1}^{N} p^{(k)}(\boldsymbol{x},t) p^{*(k)}(\boldsymbol{x},t+\tau) \end{aligned} \tag{31}$$

where the star superscript stands for complex conjugate. Replacing the pressure terms by their explicit expressions, the pressure correlation function is given by

$$\begin{aligned} R_{pp}(\boldsymbol{x},\tau) = \left(\frac{\rho_\infty c_\infty^2}{2\pi}\right)^2 \int ... \int \Pi_n(\boldsymbol{x},\boldsymbol{y_1},\omega_1) \Pi_m^*(\boldsymbol{x},\boldsymbol{y_2},\omega_2) < f_n(\boldsymbol{y_1},t_1) f_m(\boldsymbol{y_2},t_2) > \times ... \\ e^{i[\omega_1(t-t_1)-\omega_2(t+\tau-t_2)]} d\omega_1 d\omega_2 d\boldsymbol{y_1} d\boldsymbol{y_2} dt_1 dt_2 \end{aligned} \tag{32}$$

In this expression, the time variable t can take any value. It will have no influence on the final result as will be shown below. This is due to the statistical stationarity of the signals.

II.D. Estimation of the Power Spectral Density

The Power Spectral Density (PSD) is the Fourier transform of $R_{pp}(\boldsymbol{x},\tau)$. One has

$$\begin{aligned} S_{pp}(\boldsymbol{x},\omega) = \left(\frac{\rho_\infty c_\infty^2}{2\pi}\right)^2 \int ... \int \Pi_n(\boldsymbol{x},\boldsymbol{y_1},\omega_1) \Pi_m^*(\boldsymbol{x},\boldsymbol{y_2},\omega_2) < f_n(\boldsymbol{y_1},t_1) f_m(\boldsymbol{y_2},t_2) > \times ... \\ e^{i[\omega_1(t-t_1)-\omega_2(t-t_2)-(\omega+\omega_2)\tau]} d\omega_1 d\omega_2 d\boldsymbol{y_1} d\boldsymbol{y_2} dt_1 dt_2 d\tau \end{aligned} \tag{33}$$

The integration over τ and ω_2 are straightforward. Moreover, the change of variables

$$(t_1,t_2) \mapsto \begin{cases} t_1 = t_1 \\ \tau = t_2 - t_1 \end{cases} \tag{34}$$

completes the integration over t_2. The PSD is given by,

$$\begin{aligned} S_{pp}(\boldsymbol{x},\omega) = \frac{(\rho_\infty c_\infty^2)^2}{2\pi} \int ... \int \Pi_n(\boldsymbol{x},\boldsymbol{y_1},\omega_1) \Pi_m^*(\boldsymbol{x},\boldsymbol{y_2},-\omega) < f_n(\boldsymbol{y_1},t_1) f_m(\boldsymbol{y_2},t_1+\tau) > \times ... \\ e^{i[-(\omega_1+\omega)t_1+\omega_1 t+\omega(t-\tau)]} d\omega_1 d\boldsymbol{y_1} d\boldsymbol{y_2} dt_1 d\tau \end{aligned} \tag{35}$$

Since the sources are stationary, their correlation function depends only on location and time difference, i.e.

$$< f_n(\boldsymbol{y_1},t_1) f_m(\boldsymbol{y_2},t_1+\tau) > = R_{nm}(\boldsymbol{y_1},\boldsymbol{\eta},\tau) \tag{36}$$

where $\boldsymbol{\eta} = \boldsymbol{y_2} - \boldsymbol{y_1}$ is the vector joining two sources. Injecting this expression into the PSD and integrating over t_1 and ω_1 gives

$$S_{pp}(\boldsymbol{x},\omega) = (\rho_\infty c_\infty^2)^2 \int ... \int \Pi_n(\boldsymbol{x},\boldsymbol{y_1},-\omega) \Pi_m^*(\boldsymbol{x},\boldsymbol{y_1}+\boldsymbol{\eta},-\omega) R_{nm}(\boldsymbol{y_1},\boldsymbol{\eta},\tau) e^{-i\omega\tau} d\boldsymbol{y_1} d\boldsymbol{\eta} d\tau \tag{37}$$

Using an asymptotic expansion of the vector Green's functions with respect to $\boldsymbol{\eta}$, one has

$$\Pi_m^*(\boldsymbol{x},\boldsymbol{y}+\boldsymbol{\eta},-\omega) \backsimeq \Pi_m^*(\boldsymbol{x},\boldsymbol{y},-\omega) e^{i\frac{\omega}{c_\infty}\frac{\boldsymbol{x}.\boldsymbol{\eta}}{|\boldsymbol{x}-\boldsymbol{y}|}} \tag{38}$$

The exponential factor is the phase factor accounting for the retarded time difference for an observer located at $\boldsymbol{x}$ and two source terms located at $\boldsymbol{y_1}$ and $\boldsymbol{y_1}+\boldsymbol{\eta}$. Recasting this expression into the PSD,

$$S_{pp}(\boldsymbol{x},\omega) = \frac{\rho_\infty^2 \omega^2}{16\pi^2 c_\infty^2} \frac{1}{R^2} \int ... \int \frac{x_n x_m}{R^2} R_{nm}(\boldsymbol{y_1},\boldsymbol{\eta},\tau) e^{i\omega\left(\frac{1}{c_\infty}\frac{\boldsymbol{x}.\boldsymbol{\eta}}{R}-\tau\right)} d\boldsymbol{y_1} d\boldsymbol{\eta} d\tau \tag{39}$$

where $|\boldsymbol{x}-\boldsymbol{y}| \approx |\boldsymbol{x}| = R$

II.E. Estimation of the source term correlation

The initial expression for the source terms in (13b) is

$$f_i = -v_{sj}\frac{\partial v_{ti}}{\partial x_j} - v_{tj}\frac{\partial v_{si}}{\partial x_j} \tag{40}$$

Turbulence will be modeled using a classical two-equation turbulence model, for which anisotropic effeects are difficult to correctly capture. Assuming that the BBSAN source terms are isotropic appears to be a coherent level of approximation. Therefore,

$$f_i(\boldsymbol{y_1}, t) = f(\boldsymbol{y_1}, t) \text{ for } 1 \leq i \leq 3 \tag{41}$$

Dimensional analysis gives an estimate of the source terms as

$$f(\boldsymbol{y_1}, t) = \frac{p_s(\boldsymbol{y_1})v_t(\boldsymbol{y_1}, t)}{\rho_\infty c_\infty l(\boldsymbol{y_1})} \tag{42}$$

where l is the local characteristic length scale of turbulence in the streamwise direction. The source terms being isotropic, so is the correlation function. Hence $R_{nm}(\boldsymbol{y_1}, \eta, \tau) = R_{iso}(\boldsymbol{y_1}, \eta, \tau)$ for $n = m$ and there is no contribution of the terms for $n \neq m$. As a result

$$\frac{x_n x_m}{R^2} R_{nm}(\boldsymbol{y_1}, \boldsymbol{\eta}, \tau) = \frac{x_1^2 + x_2^2 + x_3^2}{R^2} R_{iso}(\boldsymbol{y_1}, \boldsymbol{\eta}, \tau) = R_{iso}(\boldsymbol{y_1}, \boldsymbol{\eta}, \tau) \tag{43}$$

Inserting (42) into (36),

$$R_{iso}(\boldsymbol{y_1}, \eta, \tau) = \frac{p_s(\boldsymbol{y_1})p_s(\boldsymbol{y_1} + \boldsymbol{\eta})}{\rho_\infty^2 c_\infty^2 l(\boldsymbol{y_1})^2} < v_t(\boldsymbol{y_1}, t_1)v_t(\boldsymbol{y_1} + \boldsymbol{\eta}, t_1 + \tau) > \tag{44}$$

where the ensemble average $< >$ applies only on unsteady terms and l was considered as constant over the distance $\boldsymbol{\eta}$. p_s will be determined directly from the RANS calculation, whereas $< v_t(\boldsymbol{y_1}, t_1)v_t(\boldsymbol{y_1} + \boldsymbol{\eta}, t_1 + \tau) >$ requires some modeling. It represents the correlation of the turbulent velocity fluctuations and is modeled by

$$R_v(\boldsymbol{y_1}, \boldsymbol{\eta}, \tau) = K(\boldsymbol{y_1}) \exp\left[-\frac{|\xi|}{u_c \tau_s} - \frac{(\xi - u_c\tau)^2}{l^2} - \frac{\gamma^2 + \zeta^2}{l_\perp^2}\right] \tag{45}$$

where $\boldsymbol{\eta} = (\xi, \gamma, \zeta)$ is the distance between two source terms, K is the turbulence kinetic energy, τ_s is the characteristic time scale of turbulence and $l_\perp$ is the characteristic length scale of turbulence in the cross stream direction, u_c is the local convection velocity. The isotropic correlation is now given by

$$R_{iso}(\boldsymbol{y_1}, \boldsymbol{\eta}, \tau) = K(\boldsymbol{y_1})\frac{p_s(\boldsymbol{y_1})p_s(\boldsymbol{y_1} + \boldsymbol{\eta})}{\rho_\infty^2 c_\infty^2 l(\boldsymbol{y_1})^2} \exp\left[-\frac{|\xi|}{u_c \tau_s} - \frac{(\xi - u_c\tau)^2}{l^2} - \frac{\gamma^2 + \zeta^2}{l_\perp^2}\right] \tag{46}$$

The PSD is determined by casting (46) into (39) and integrating over τ at fixed ξ, giving

$$\begin{aligned} S_{pp}(\boldsymbol{x}, \omega) = \frac{\omega^2}{16\pi\sqrt{\pi} c_\infty^4 R^2} \int ... \int \frac{K}{l u_c} \exp\left(-\frac{\omega^2}{4}\frac{l^2}{u_c^2}\right) p_s(\boldsymbol{y}) p_s(\boldsymbol{y} + \boldsymbol{\eta}) \times ... \\ \exp\left(-i\frac{\omega\xi}{u_c}\right) \exp\left[-\frac{|\xi|}{u_c\tau_s} - \frac{\gamma^2 + \zeta^2}{l_\perp^2}\right] \exp\left(i\frac{\omega}{c_\infty}\frac{x_1\xi + x_2\gamma + x_3\zeta}{R}\right) d\boldsymbol{\eta} d\boldsymbol{y} \end{aligned} \tag{47}$$

II.F. Numerical Implementation

Equation (47) consists in a double spatial integral over the BBSAN source domain, that is the jet flow. The numerical computation of this expression requires some inputs from a RANS calculation. Following Tam and Auriault,[17] the characteristic time scale is given by $\tau_s = c_\tau K/\varepsilon$ where ε is the dissipation of the turbulent kinetic energy and c_τ is a constant. The length scales are given by $l = c_l K^{3/2}/\varepsilon$ and $l_\perp = c_\perp l$ where c_l and $c_\perp$ are two constants. The shock pressure p_s is given by subtracting the ambient pressure to the computed static pressure in the jet. The convection velocity is approximated by the local mean velocity.

At this stage, the main difference with Morris and Miller's model[10] is that the Fourier transform of the static pressure along the x_1 direction $\tilde{p}_s(k_1, y_2, y_3)$ has not been used here. Morris and Miller argued that this resulted in a simpler numerical implementation, which is true, because it simplifies the final expression for the PSD: the PSD here requires the evaluation of 6 spatial integrals, whereas Morris and Miller only use 3 spatial integrals and one along the wave number k_1 of $\tilde{p}_s$.

It should be noted that computing the Fourier transform $\tilde{p}_s$ with a fast algorithm such as FFT requires an equally spaced mesh in the x_1 direction. If the original CFD mesh does not meet this requirement, it is possible to interpolate the original mesh to a regular grid, as Morris and Miller did. Consequently, Morris and Miller approach is probably more efficient for academic configurations. On the other hand, industrial geometries are dual-stream and include a plug (a cone-shaped part in the center of the primary flow). Then secondary flow is not parallel to x_1 but follows the plug slopes.

The correlation function used here also differs from the one proposed by Morris and Miller. It is expected to give similar results, but provides a simpler expression of the PSD when the spatial Fourier transform is not used.

III. Results on single-stream jets

Single-stream jets are typical academic configurations. A thorough test campaign has been conducted at Ecole Centrale de Lyon by André et al.[1,18,19] to characterize BBSAN and flight effects. Measurements include aerodynamic quantities (static pressure, Particle Injection Velocimetry, Schlieren imaging) as well as acoustic data (near and far field spectra).

First, the aerodynamic calculations are compared with measurements to ensure the validity of the inputs given to the model. Then, the results of the model are compared with the measured spectra for several jet Mach number M_j and observation angles.

III.A. Aerodynamic results

The RANS calculations were done with the elsA CFD solver developed by ONERA. A spatial Roe scheme was used and turbulence was modeled using a $k-\omega-SST$ model.[20–22]

The same nozzle geometry was used for measurements and calculations. It is a convergent-divergent nozzle, the design Mach number is $M_d = 1.3$ and the exit diameter is $D = 0.038$m. The jet is cold.

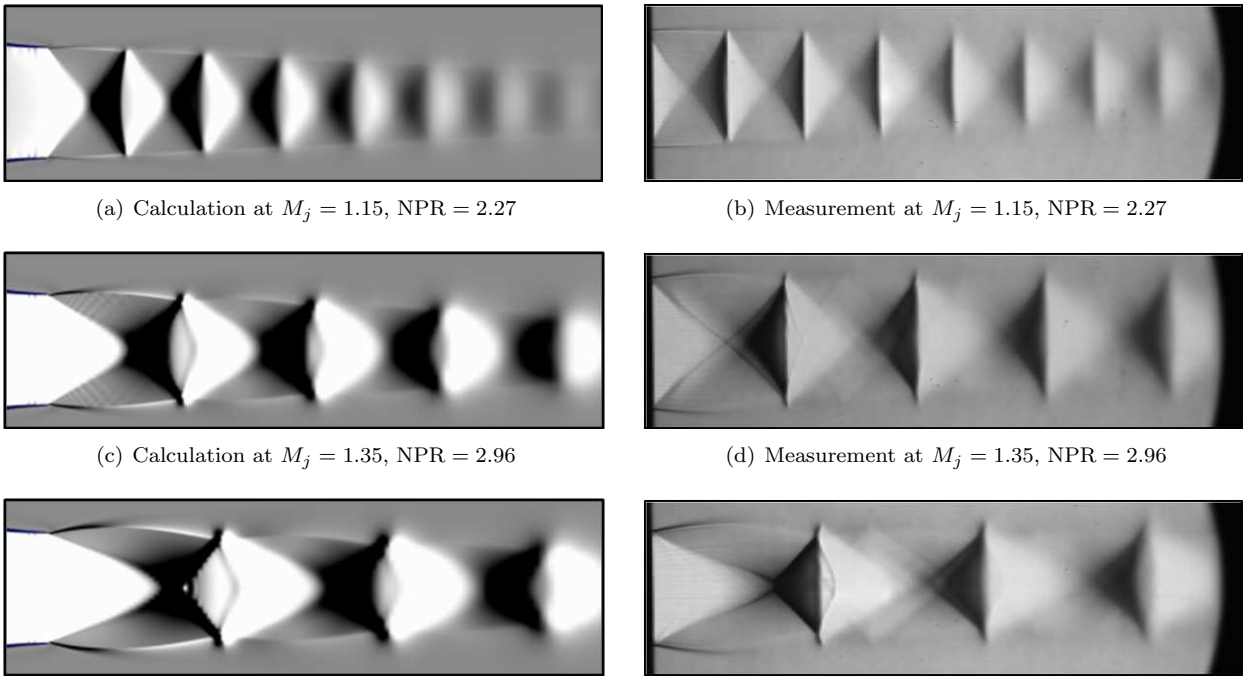

(a) Calculation at $M_j = 1.15$, NPR $= 2.27$

(b) Measurement at $M_j = 1.15$, NPR $= 2.27$

(c) Calculation at $M_j = 1.35$, NPR $= 2.96$

(d) Measurement at $M_j = 1.35$, NPR $= 2.96$

(e) Calculation at $M_j = 1.5$, NPR $= 3.67$

(f) Measurement at $M_j = 1.5$, NPR $= 3.67$

Figure 2. Comparison of numerical and experimental Schlieren visualisations for different jet Mach number

The qualitative features of the jet are easily studied through Schlieren visualizations. This optical technique reflects the density gradients in the jet and is particularly suited for shocked jets. Numerically, it is simulated by computing the norm of the density gradient. Comparisons are shown in figure 2. The overall agreement is very good. In Figures 2(a) and 2(b) a slightly underexpanded jet at $M_j = 1.15$ is presented. The shock-cell structure is clearly visible: it consists in a series of expansion fans and compression cells, the strength of which decreases as moving downstream. When the jet Mach number is increased to $M_j = 1.35$, the shock-cells lengthens as shown in Figures 2(c) and 2(d). The jet sonic line bends creating a barrel-like pattern for the shock-cells. In Figures 2(e) and 2(f), a strongly underexpanded jet at $M_j = 1.5$ is presented. A Mach disc forms in the first shock-cell as seen in figure 2(f).

According to equation (47), the key aerodynamic quantities used to predict BBSAN are the shock pressure p_s, the convection velocity u_c and the turbulent variables. The study of the jet static pressure is an essential quantitative information. The comparison of calculations with measurements in Figure 3 shows an excellent agreement. The shock locations are correctly predicted by the calculation. The trend in amplitude decay is similar between measurements and calculations, though the CFD solution seems to slightly overestimate the shock damping. Numerical dissipation is probably responsible for this difference. It should be noted that the presence of shocks in the jet flow requires some numerical dissipation to be added on purpose. The numerical dissipation used should be strong enough to ensure the convergence of the calculation, but as low as possible not to flatten the shocks.

For $x/D > 6$, p_s/p_∞ tends to unity in the calculations and to a lower value experimentally, which may look surprising. This difference probably stems from the pressure probe: it is designed to work at supersonic Mach numbers, and for $x/D > 6$ the flow becomes transonic. Hence, far downstream the probe is out of its operating range, which explains the difference.

The case $M_j = 1.35$ contains stronger shocks as evidenced in Figure 4. Both expansion fans and compression shocks are stronger than in the $M_j = 1.15$ case. Comparison with Figure 3 shows that shock cells lengthens with Mach number, as expected.

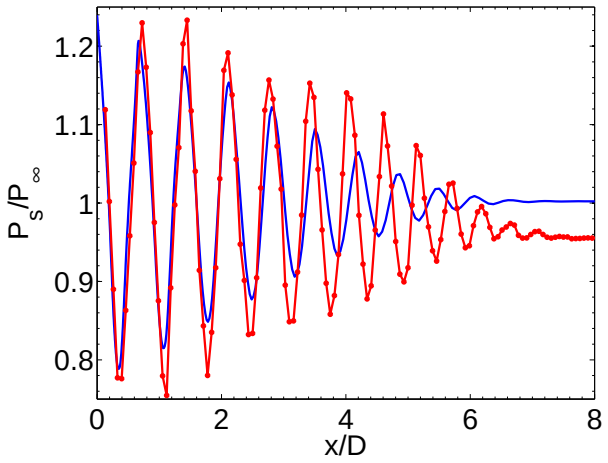

Figure 3. Static pressure on the jet axis, $M_j = 1.15$. calculations, measurements

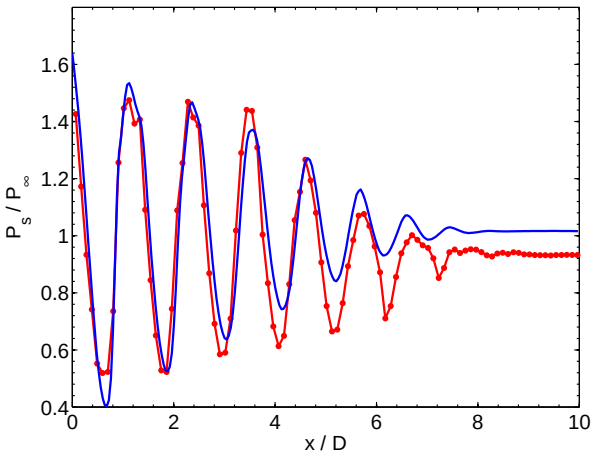

Figure 4. Static pressure on the jet axis, $M_j = 1.35$. calculations, measurements

III.B. Acoustic results

The first results given in Figure 5 concern a jet at $M_j = 1.15$. This Mach number is a typical value of the secondary stream of a civil engine. The PSDs were computed using (47). A Strouhal representation is used: let $f_c = u_j/D$ be a characteristic frequency of the jet, then the frequencies (in Hertz) are divided by f_c to get a Strouhal representation. A $10 \log_{10} f_c$ factor is added to the PSDs: the PSDs are in dB/St and energy is thus preserved.

Four observation angles Φ (inlet angle, $\Phi = \pi - \theta$) were computed, from the upstream to the downstream direction. The first encouraging result is that the peak frequency is correctly captured numerically for all observer locations: f_p increases with inlet angle, both experimentally and numerically. Experimentally, the emergence of BBSAN diminishes as Φ increases, which is also the case with the computations. On

quantitative grounds, the shape of the hump is generally well captured, especially for $\Phi = 70°$ (see Figure 5(b)) and $\Phi = 90°$ (see Figure 5(c)).

The fact that the calculated PSDs agree well with measurements for low frequencies ($St < 0.5$ for $\Phi = 50°$) is a coincidence: at such low frequencies, mixing noise is dominant and the model is not expected to account for mixing noise.

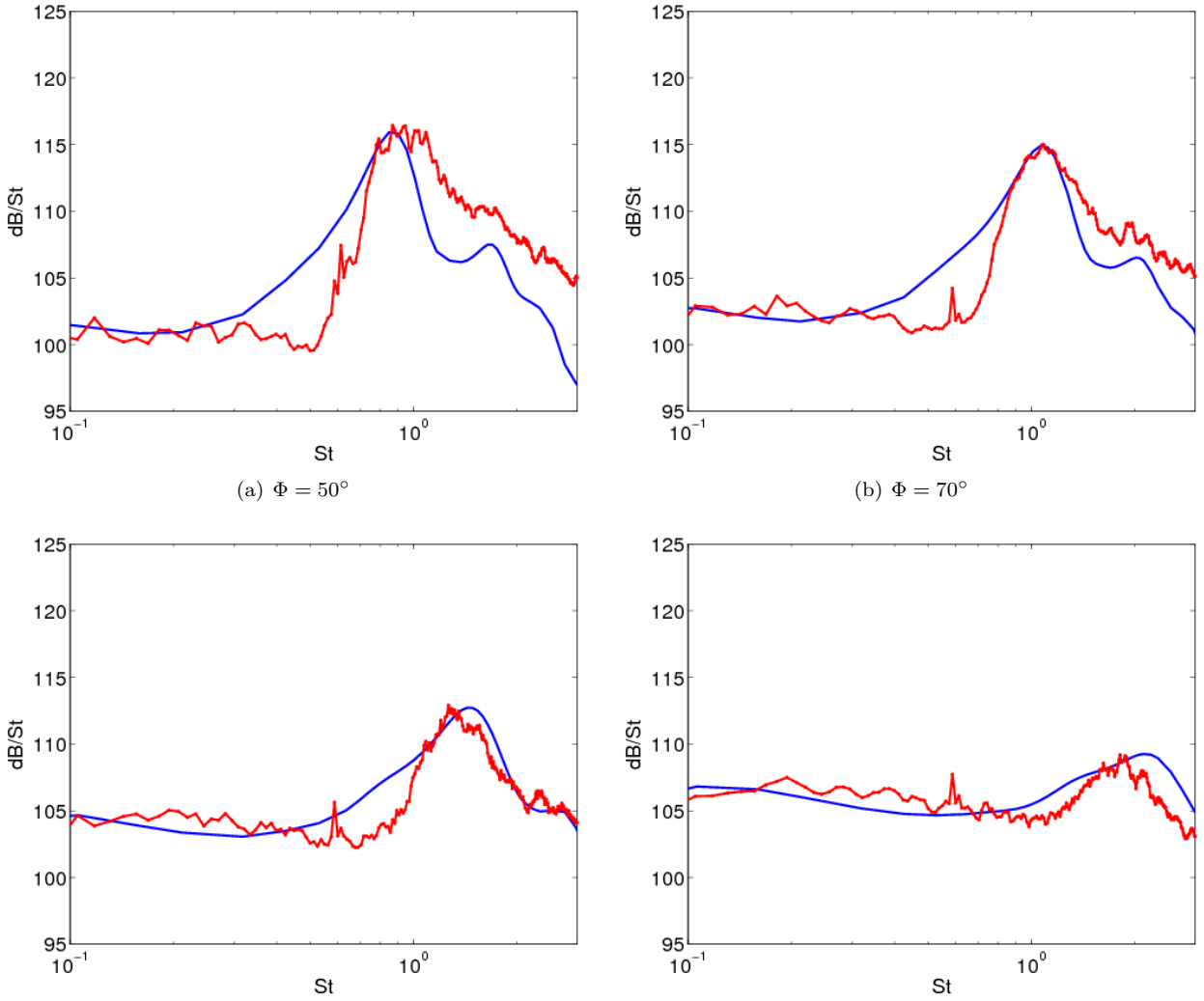

(a) $\Phi = 50°$ (b) $\Phi = 70°$

(c) $\Phi = 90°$ (d) $\Phi = 110°$

Figure 5. PSDs of a shocked jet, $M_j = 1.15$ for various observer locations. Φ is the inlet angle. —— Measurements by André et al., —— Calculations

The case of a jet at $M_j = 1.35$ is now considered. It is presented in Figure 6. As compared to the $M_j = 1.15$ case, BBSAN is expected to peak at lower frequencies because of longer shock-cells due to the increased jet Mach number. According to measurements, at $\Phi = 50°$, $f_p/f_c = 1$ at $M_j = 1.15$ and $f_p/f_c = 0.5$ at $M_j = 1.35$. This was expected. Another interesting feature of this higher M_j case, is that multiple peaks become more visible especially at $\Phi = 50°$ and $\Phi = 70°$.

The aforementioned changes are well captured by the model: the peak frequency is lower than in the $M_j = 1.15$ case and the general shape of the spectrum agrees reasonably well with measurements. The multiple peaks in the spectrum are also predicted, though their amplitude decays a bit too fast.

IV. Inclusion of refraction effects

So far, the free field Green's functions were used hence neglecting the potential refraction effects of the acoustic waves by the mean flow. In this part, it is proposed to account for refraction effects using geometric

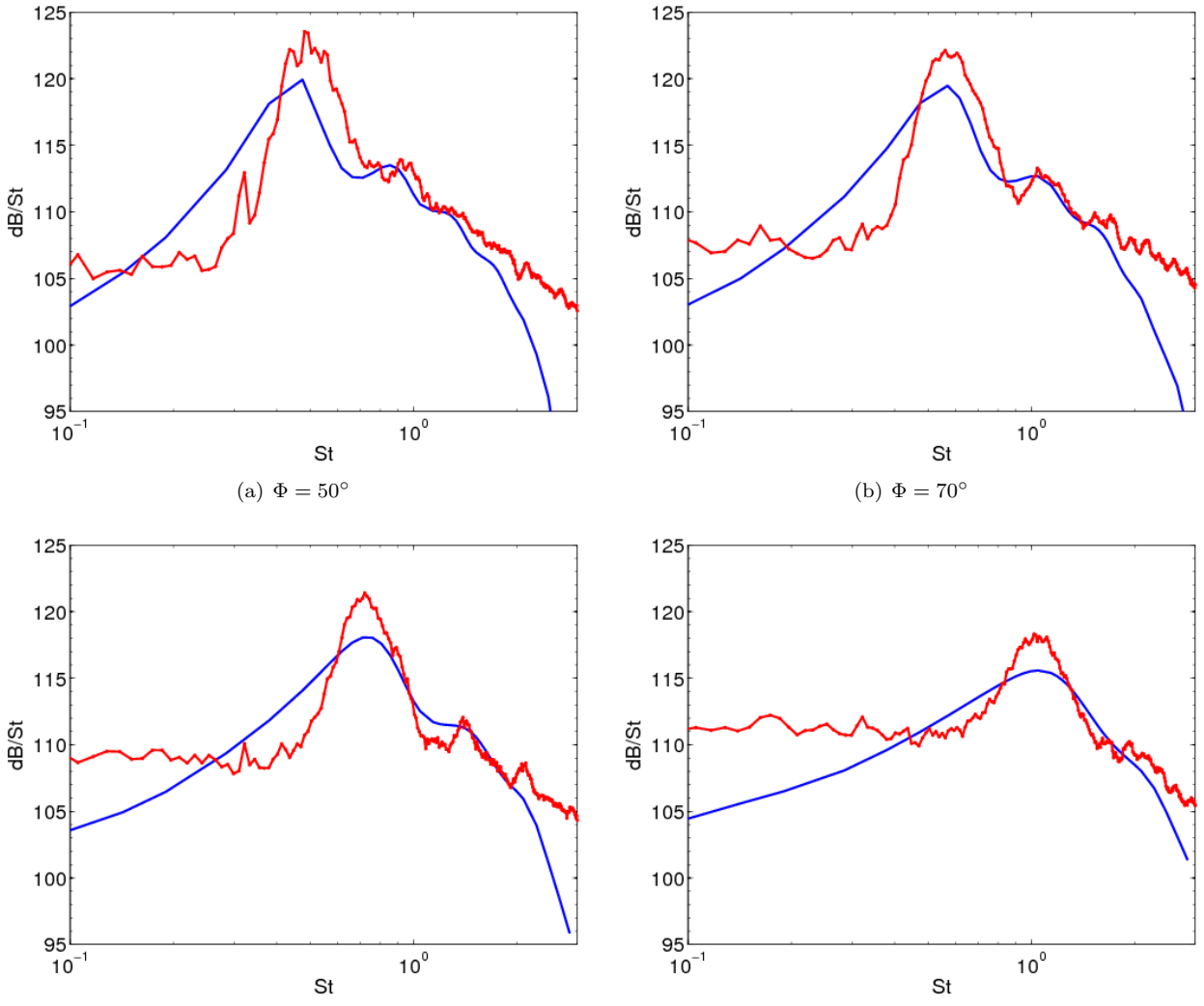

(a) $\Phi = 50°$ (b) $\Phi = 70°$

(c) $\Phi = 90°$ (d) $\Phi = 110°$

Figure 6. PSDs of a shocked jet, $M_j = 1.35$ for various observer locations. Φ is the inlet angle. —— Measurements by André et al., —— Calculations

acoustics. First, two simple examples are presented to illustrate the refraction phenomenon on a commercial engine. Secondly, the ray-tracing theory is briefly recalled. It is used in the third part, where a formal relation between the Green's functions and the acoustic rays is derived.

IV.A. Refraction on a dual-stream jet

Before accounting for the phenomenon, it seems interesting to mention where it takes place. BBSAN sources are located where shock-cells and turbulence interact, that is in the mixing layers. On a commercial civil engine, the secondary stream is shocked while the primary stream is subsonic. As a result, BBSAN sources are located in the mixing layer between the primary and secondary flow (PS sources), as well as in the mixing region between the secondary and external flow (SE sources).

In Figures 7-8, the radiation pattern of both types of sources is presented on a civil configuration. It involves a dual-stream geometry with no external flow. A source is placed inside the mixing layer and acoustic rays (in white) are shot from the source. The bending of the ray accounts for refraction effects. An example of SE source radiation is shown in Figure 7. In this case, acoustic rays undergo slight refraction effects. Neglecting refraction effects for these sources could appear as a reasonable approximation. The case of PS sources is illustrated in Figure 8. The acoustic rays shot from the source are strongly refracted by the mixing layer between the secondary and external stream. Refraction cannot be neglected in this present case.

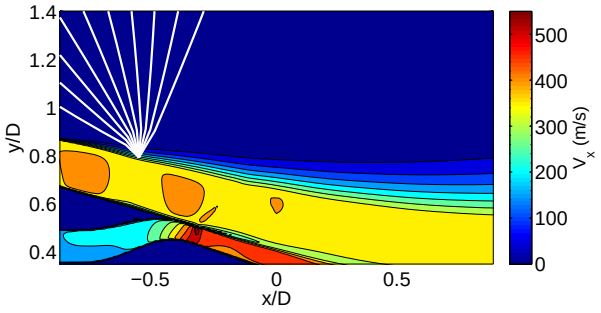

Figure 7. Radiation of a SE source

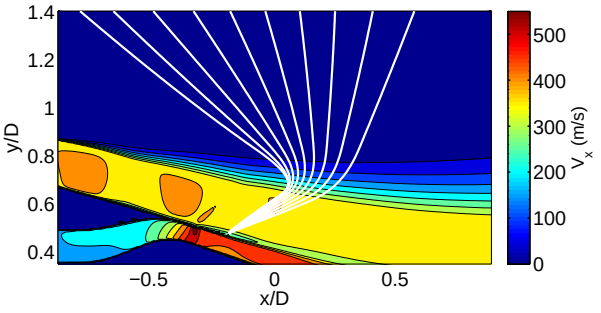

Figure 8. Radiation of a PS source

To circumvent this issue, Morris and Miller[13] numerically computed the vector Green's functions associated with the LEE. The problem is mathematically and numerically complex and a simpler approach is described here. A ray-tracing algorithm is used to account for refraction effects. A high-frequency approximation of the Green's functions may be derived directly from ray-tracing.

IV.B. The ray-tracing method

The basics of the ray-tracing method used in the remaining of the paper are briefly recalled. The ray-tracing approach provides a high-frequency solution to the LEE. It is similar to a multiple scale resolution of the LEE. Physically, the acoustic waves are locally described as plane waves. Ray paths are tangent to the group velocity and indicate the propagation of acoustic energy. The ray paths are obtained by solving the eikonal equations

$$\begin{cases} \dfrac{dx_i}{dt} = c\dfrac{k_i}{k} + v_{0i} \equiv g_i(\boldsymbol{x}, \boldsymbol{k}) \\ \dfrac{dk_i}{dt} = -k\dfrac{\partial c}{\partial x_i} - k_j \dfrac{\partial v_{0j}}{\partial x_i} \equiv h_i(\boldsymbol{x}, \boldsymbol{k}) \end{cases} \tag{48}$$

where $\boldsymbol{x}$ is the ray trajectory as a function of time, $\boldsymbol{k}$ is the wave vector, $k = ||\boldsymbol{k}||$. The initial conditions are the source location and the shooting angles (θ_0, α_0). The formulation adopted here is provided by Candel.[23] The coordinate system is described in Figure 9. The acoustic flux is conserved in a ray tube

$$\int_S E\boldsymbol{v_g}.\boldsymbol{n}dS = 0 \tag{49}$$

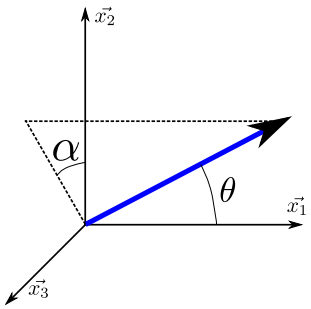

Figure 9. Coordinate system used for ray-tracing. x_1 is the jet axis, the ray is shown in blue

where E is acoustic energy density ($J.m^{-3}$), dS is the elementary surface of the ray tube cross-section, $\boldsymbol{n}$ is the normal vector to dS and $\boldsymbol{v_g}$ is the group velocity vector. The local interpretation of (49) is

$$E\boldsymbol{v_g}\cdot\boldsymbol{n}dS = \boldsymbol{I}\cdot\boldsymbol{n}dS = K_1 \tag{50}$$

where $\boldsymbol{I}$ is the acoustic intensity vector and K_1 is a constant equal to the acoustic power injected by the source in the ray tube. In the particular case of an isotropically radiating source

$$K_1 = \frac{d\Omega}{4\pi}W_a \tag{51}$$

where $d\Omega$ is the solid angle associated with the ray tube and W_a is the source power. $\boldsymbol{I}$ being collinear to the ray paths, one has

$$I = \frac{K_1}{dS} \tag{52}$$

To track the evolution of dS along the ray paths, Candel[23] introduced the following geodesic elements

$$\begin{cases} \boldsymbol{R}^\theta = \left(\dfrac{\partial \boldsymbol{x}}{\partial\theta_0}\right)_{t,\alpha_0} & \boldsymbol{R}^\alpha = \left(\dfrac{\partial \boldsymbol{x}}{\partial\alpha_0}\right)_{t,\theta_0} \\ \boldsymbol{Q}^\theta = \left(\dfrac{\partial \boldsymbol{k}}{\partial\theta_0}\right)_{t,\alpha_0} & \boldsymbol{Q}^\alpha = \left(\dfrac{\partial \boldsymbol{k}}{\partial\alpha_0}\right)_{t,\theta_0} \end{cases} \tag{53}$$

$\boldsymbol{R^\theta}$ quantifies the change in the ray path when slightly shifting the shooting angle θ_0. By applying the chain rule of differentiation, the evolution of the geodesic elements is governed by

$$\begin{cases} \dfrac{d\boldsymbol{R}}{dt} = \dfrac{\partial \boldsymbol{g}}{\partial \boldsymbol{x}}\cdot\boldsymbol{R} + \dfrac{\partial \boldsymbol{g}}{\partial \boldsymbol{k}}\cdot\boldsymbol{Q} \\ \dfrac{d\boldsymbol{Q}}{dt} = \dfrac{\partial \boldsymbol{h}}{\partial \boldsymbol{x}}\cdot\boldsymbol{R} + \dfrac{\partial \boldsymbol{h}}{\partial \boldsymbol{k}}\cdot\boldsymbol{Q} \end{cases} \tag{54}$$

After solving systems (48) and (54), the divergence or convergence of the rays is easily evaluated by

$$dS = |(d\theta_0\boldsymbol{R}^\theta)\times(d\alpha_0\boldsymbol{R}^\alpha)\cos(\boldsymbol{k},\boldsymbol{v_g})| \tag{55}$$

and I is then determined by (52). The ray-tracing algorithm can provide the acoustic pressure evolution in the flow from a fixed source term. Intuitively, this is closely related to the general definition of a Green's function. This point is established in the next section.

IV.C. Formal relation between Green's functions and acoustic rays

The source terms lie in the mixing layer and radiate to the observer in the acoustic far field. It is assumed that the mean flow is uniformly sheared and parallel to the jet axis, so that

$$\overline{\boldsymbol{v}} = (\overline{v}_1(x_2,x_3),0,0) \tag{56}$$

As shown by Lilley,[24] it is possible to combine the Euler equations to form a third-order wave equation. The interpretation of all the source terms on the right-hand side of this equation is however tricky.[25] It is possible to linearize this equation about the mean state, so that Lilley's equation reduces to[26,27]

$$\mathcal{L}p' = \frac{D}{Dt}\left(\frac{D^2}{Dt^2} - \nabla\cdot\bar{c}^2\nabla\right)p' + 2\bar{c}^2\nabla\overline{v_1}\cdot\nabla\frac{\partial}{\partial x_1}p' = \overline{\rho}\,\bar{c}^2\Gamma \tag{57}$$

where Γ is the source term defined by

$$\Gamma \equiv \frac{D}{Dt}\nabla\cdot\boldsymbol{f} - 2\nabla\overline{v}_1\cdot\frac{\partial}{\partial x_1}\boldsymbol{f} \tag{58}$$

In (57) the assumption that $\overline{\rho}\,\bar{c}^2 = \gamma\overline{p}$ has been made. Indeed, the uniform shear flow hypothesis implies that the mean static pressure $\overline{p}$ is constant.

The Green's function associated with $\mathcal{L}$, namely g_L, satisfies

$$\mathcal{L}g_L(\boldsymbol{x},\boldsymbol{y},\omega) = \delta(\boldsymbol{x}-\boldsymbol{y}) \tag{59}$$

so that the solution to (57) is

$$p'(\boldsymbol{x},\omega) = \overline{\rho}\,\bar{c}^2\int g_L(\boldsymbol{x},\boldsymbol{y},\omega)\Gamma(\boldsymbol{y},\omega)d\boldsymbol{y} \tag{60}$$

The source term is given by

$$\Gamma(\boldsymbol{y},\omega) = \left(-i\omega + \overline{v}_1\frac{\partial}{\partial y_1}\right)\frac{\partial f_i}{\partial y_i} - 2\frac{\partial\overline{v}_1}{\partial y_i}\frac{\partial f_i}{\partial y_1} \tag{61}$$

Injecting (61) into (60) and performing some algebra leads to

$$\begin{aligned} p'(\boldsymbol{x},\omega) =& \overline{\rho}\,\bar{c}^2\int\left[\left(i\omega\frac{\partial g_L}{\partial y_1} + \overline{v}_1\frac{\partial^2 g_L}{\partial y_1^2}\right)f_1 + \left(i\omega\frac{\partial g_L}{\partial y_2} + 3\frac{\partial\overline{v}_1}{\partial y_2}\frac{\partial g_L}{\partial y_1} + \overline{v}_1\frac{\partial^2 g_L}{\partial y_1\partial y_2}\right)f_2\right. \\ &\left. + \left(i\omega\frac{\partial g_L}{\partial y_3} + 3\frac{\partial\overline{v}_1}{\partial y_3}\frac{\partial g_L}{\partial y_1} + \overline{v}_1\frac{\partial^2 g_L}{\partial y_1\partial y_3}\right)f_3\right]d\boldsymbol{y} \end{aligned} \tag{62}$$

Comparing (62) with the general solution

$$p'(\boldsymbol{x},\omega) = \overline{\rho}\,\bar{c}^2\iint\Pi_n(\boldsymbol{x},\boldsymbol{y},\omega)f_n(\boldsymbol{y},\omega)d\boldsymbol{y} \tag{63}$$

gives the analytical expressions of the vector Green's functions, namely

$$\begin{aligned} \Pi_1(\boldsymbol{x},\boldsymbol{y},\omega) &= i\omega\frac{\partial g_L}{\partial y_1} + \overline{v}_1\frac{\partial^2 g_L}{\partial y_1^2} \\ \Pi_2(\boldsymbol{x},\boldsymbol{y},\omega) &= i\omega\frac{\partial g_L}{\partial y_2} + 3\frac{\partial\overline{v}_1}{\partial y_2}\frac{\partial g_L}{\partial y_1} + \overline{v}_1\frac{\partial^2 g_L}{\partial y_1\partial y_2} \\ \Pi_3(\boldsymbol{x},\boldsymbol{y},\omega) &= i\omega\frac{\partial g_L}{\partial y_3} + 3\frac{\partial\overline{v}_1}{\partial y_3}\frac{\partial g_L}{\partial y_1} + \overline{v}_1\frac{\partial^2 g_L}{\partial y_1\partial y_3} \end{aligned} \tag{64}$$

These equations relate the scalar Green's function of Lilley's equation g_L, to the vector Green's functions Π_n of the LEE.

The last step is to determine $g_L(\boldsymbol{x},\boldsymbol{y},\omega)$ from the ray-tracing method. The starting point is to shoot from $\boldsymbol{y}$ at $\boldsymbol{x}$ and to compute the conservative quantities along the ray. To properly scale the Green's function computed, the acoustic power to inject in the ray tubes has to be determined first. The Green function $g_L(\boldsymbol{x},\boldsymbol{y},\omega)$ is the pressure field created by a source term $S(\boldsymbol{x}) = \delta(\boldsymbol{x}-\boldsymbol{y})$. The total acoustic power W_a radiated by the elementary source S is computed in the absence of a mean flow, on a sphere of radius unity

$$W_a = \int\boldsymbol{I}\cdot\boldsymbol{n}dS \tag{65}$$

The pressure field is given by

$$p'(\boldsymbol{x},t) = -\frac{e^{-i\frac{\omega}{c_\infty}R}}{4\pi R}e^{-i\omega t} \tag{66}$$

where $R = ||\boldsymbol{x}||$. Recalling that $I = \overline{p'^2}/\rho_\infty c_\infty$, one has

$$\overline{p'^2}(\boldsymbol{x}) = \frac{1}{32\pi^2 R^2} \quad I = \frac{1}{32\pi^2\rho_\infty c_\infty R^2} \quad \text{and} \quad W_a = \frac{1}{8\pi\rho_\infty c_\infty} \tag{67}$$

The conservation of the acoustic flux through a ray tube gives

$$\overline{p'^2} = \frac{\rho c^2 K_1}{(1+\boldsymbol{M}.\boldsymbol{\nu})\boldsymbol{v_g}\cdot d\boldsymbol{S}} \tag{68}$$

Under the high-frequency hypothesis, the acoustic pressure is expressed as

$$p'(\boldsymbol{x},t) = \tilde{p}(\boldsymbol{x})e^{i(\boldsymbol{k}\cdot\boldsymbol{x}-\omega t)} \tag{69}$$

The complex amplitude $\tilde{p}(\boldsymbol{x})$ is related to the RMS value of p' by

$$\tilde{p}(\boldsymbol{x}) = \pm\sqrt{\frac{2\rho c^2 K_1}{(1+\boldsymbol{M}.\boldsymbol{\nu})\boldsymbol{v_g}\cdot d\boldsymbol{S}}} \tag{70}$$

The Green's function g_L is then given by

$$g_L(\boldsymbol{x},\boldsymbol{y},\omega) = -\sqrt{\frac{2\rho c^2 K_1}{(1+\boldsymbol{M}.\boldsymbol{\nu})\boldsymbol{v_g}\cdot d\boldsymbol{S}}}\, e^{i\boldsymbol{k}\cdot\boldsymbol{x}} \tag{71}$$

This expression supposes that K_1 (the acoustic power injected in the ray tube) as well as the value of W_a have been calculated using (51) and (67) respectively.

An example of the calculation of g_L is now given. The particular case of a quiescent medium is presented in Figure 10 for verification: the source is located at the origin, the ray is shot at $\theta_0 = 45°$, the source pulsation is set to $\omega_0 = 2\pi \times 10000$rad/s and the evolution of $g_L(\boldsymbol{x}, 0, \omega_0)$ versus $\boldsymbol{x}/\lambda$ is shown in Figure 10. λ is the wavelength defined by $\lambda = \frac{2\pi c}{\omega}$. The function g_L computed by the ray-tracing method is compared to the analytical free field Green's function and a perfect agreement is found.

As a second example, the case of a uniform flow parallel to the x_1 direction, with $v_1 = 200$m/s, is reported in Figure 11. The Green's function g_L is compared to the analytical Green's function given by Howe[28] and a perfect agreement is again observed.

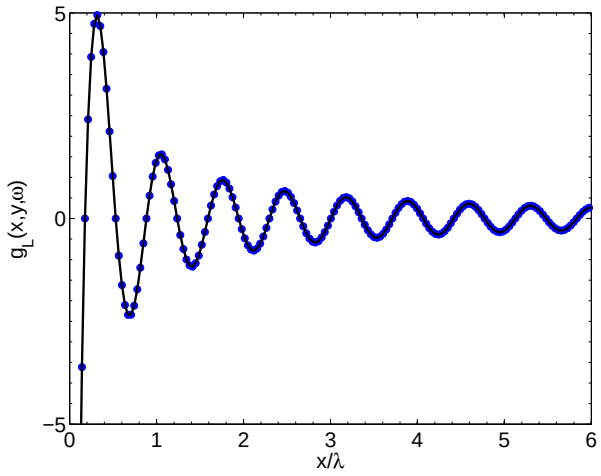

Figure 10. Numerical calculation of the Green's function without mean flow. —— analytical solution. ● ray solution. Shooting angle $\theta_0 = 45$ deg

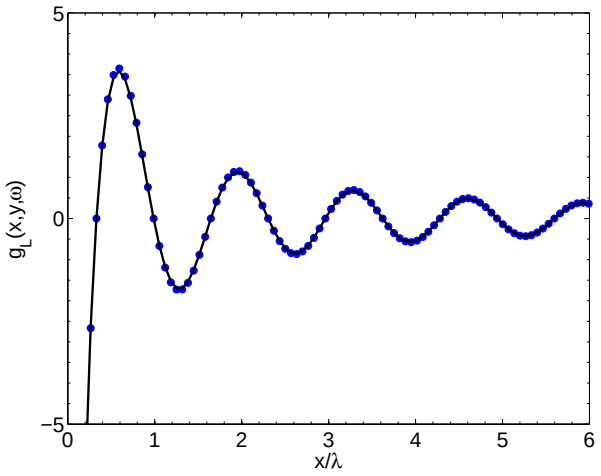

Figure 11. Numerical calculation of the Green's function with a uniform mean flow $\overline{v}_1 = 200m/s$. —— analytical solution. ● ray solution. Shooting angle $\theta_0 = 45$ deg

IV.D. Numerical implementation of refraction effects

To account for refraction effects, the vector Green's functions of the LEE $\Pi_n(\boldsymbol{x}, \boldsymbol{y}, \omega)$ need to be evaluated. This requires the knowledge of the Green's function of Lilley's equation $g_L(\boldsymbol{x}, \boldsymbol{y}, \omega)$, and its first and second order derivatives along $\boldsymbol{y}$ as expressed in (64).

The function $g_L(\boldsymbol{x}, \boldsymbol{y}, \omega)$ is determined by shooting from $\boldsymbol{y}$ at the observer $\boldsymbol{x}$ as explained above. Its first and second order derivatives are computed with finite differences, by shooting from points close to the source location. For instance, to compute $\partial g_L / \partial y_1$ at first order, one shoots from $\boldsymbol{y}$ and from $\boldsymbol{y} + dy\boldsymbol{e}_1$, where dy is a small spatial step and $\boldsymbol{e}_1$ is a unit vector in the x_1 direction.

The direct determination of eigen rays between a couple source at $\boldsymbol{x}$ and receiver at $\boldsymbol{y}$ is not very efficient. A more efficient approach consists in preliminarily solving the adjoint problem, as suggested by Tam.[29] The adjoint problem is obtained by reversing the mean flow, that is $\overline{\boldsymbol{v}}$ in the direct problem becomes $-\overline{\boldsymbol{v}}$ in the adjoint problem. The fundamental property is that ray paths will have the same trajectory in both problems (direct and adjoint). An example of application is given in Figure 12. A Gaussian velocity profile is used for the mean shear flow

$$v_1(y) = 0.58 c_\infty \exp(-y^2/(5D^2)) \tag{72}$$

The velocity profile is drawn on the left side of the figure. On the right side, the ray paths are plotted. The black circles represent 3 observers and the 2 red circles represent two source terms. For a given source-observer pair, the computation of $g_L(\boldsymbol{x}, \boldsymbol{y}, \omega)$ is achieved like this: first consider the adjoint problem. Shoot from the observer at the source in all directions (black rays in Figure 12). Determine the closest ray to the source and its angle of intersection: this is θ_0. Then shoot back at the observer in the direct problem (red ray in Figure 12), using θ_0 determined in the adjoint problem. The equivalence of the direct and adjoint problem is clearly illustrated in Figure 12: the rays do follow the same trajectories in both problems. The strong effect of the flow on the rays is also evidenced: rays bend away from the jet axis, and produce the so-called cone of silence.

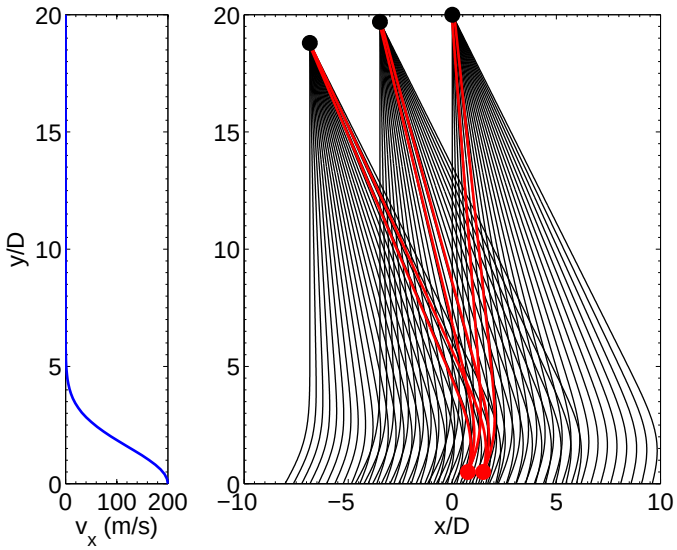

Figure 12. Ray-tracing in the direct and adjoint problems. ● observer, ● source, —— adjoint ray, —— direct ray

V. Conclusion

The objective of this work was to develop a model for BBSAN, applicable to complex configurations, and informed by a RANS simulation. Neglecting refraction effects at first, this model has been successfully validated on a single-stream jet at two operating conditions and for various observation angles.

A methodology to include refraction effects using geometric acoustics has then been developed. The Green's function of Lilley's equation is estimated by ray-tracing, and then related to the vector Green's functions of the LEE. The numerical calculation of the scalar Green's function has been validated.

The computation of the vector Green's functions and their coupling with the initial prediction model will be done in the near future, enabling predictions on more complex dual-stream configurations with external flow.

Acknowledgments

The authors are grateful for conversations with Prof. Phil Morris. The authors would also like to thank Benoît André for the sharing of his experimental results.

References

[1]B. André, T. Castelain, and C. Bailly. Experimental exploration of an underexpanded supersonic jet. In *28th International Symposium on Shock Waves*, number 1, Manchester, 2011.

[2]J. Berland, C. Bogey, and C. Bailly. Numerical study of screech generation in a planar supersonic jet. *Physics of Fluids*, 19(7), 2007.

[3]M. Harper-Bourne and M.J. Fisher. The noise from shock waves in supersonic jets. In *AGARD Noise Mech. 13 p (SEE N74-22640 14-02); International Organization*, 1973.

[4]C.K.W. Tam and H.K. Tanna. Shock associated noise of supersonic jets from convergent-divergent nozzles. *Journal of Sound and Vibration*, 81:337–358, 1982.

[5]C.K.W. Tam. Stochastic model theory of broadband shock associated noise from supersonic jets. *Journal of Sound and Vibration*, 116:265–302, 1987.

[6]C.K.W. Tam, N.N. Pastouchenko, and K. Viswanathan. Broadband shock-cell noise from dual stream jets. *Journal of Sound and Vibration*, 324(3-5):861–891, July 2009.

[7]C. Bailly and S. Candel. Prediction of supersonic jet noise from a statistical acoustic model and a compressible turbulence closure. *Journal of Sound and Vibration*, 194(2):219–242, July 1996.

[8]C. Bailly, S. Candel, and P. Lafon. Subsonic and supersonic jet noise predictions from statistical source models. *AIAA Journal*, 35(11):1688–1696, November 1997.

[9]P.J. Morris and F. Farassat. On the acoustic analogy and alternative theories of jet noise prediction. *AIAA Journal*, 40(4):671–680, 2002.

[10]P.J. Morris and S.A.E Miller. The prediction of broadband shock-associated noise using RANS CFD. In *15th AIAA Aeroacoustics Conference*, 2009.

[11]P.J. Morris and S.A.E Miller. Prediction of broadband shock-associated noise using Reynolds-Averaged Navier-Stokes computational fluid dynamics. *AIAA Journal*, 48(12), 2010.

[12]S.A.E Miller and P.J. Morris. The prediction of broadband shock-associated noise from dualstream and rectangular jets using RANS CFD. In *16th AIAA/CEAS Aeroacoustics Conference*, 2010.

[13]S.A.E Miller and P.J. Morris. The prediction of broadband shock-associated noise including propagation effects. In *17th AIAA/CEAS Aeroacoustics Conference*, number June, pages 05 – 08, 2011.

[14]O.M. Phillips. On the generation of sound by supersonic turbulent shear layers. *Journal of Fluid Mechanics*, 9(1):1–28, 1960.

[15]S.K. Lele. Phased array models of shock-cell noise sources. In *AIAA Aeroacoustics Conference*, number May, pages 23–25, 2005.

[16]D.G. Duffy. *Green's functions with applications*. 1st edition, 2001.

[17]C.K.W. Tam and L. Auriault. Jet mixing noise from fine-scale turbulence. *AIAA Journal*, 37(2):145–153, 1999.

[18]B. André, T. Castelain, and C. Bailly. Experimental study of flight effects on screech in underexpanded jets. *Physics of Fluids*, 23(12):1–14, 2011.

[19]B. André, T. Castelain, and C. Bailly. Experimental study of flight effects on screech in underexpanded jets. In *17th AIAA/CEAS Aeroacoustics Conference*, Portland, Oregon, USA, 2011.

[20]F.R. Menter. Two-equation eddy-viscosity turbulence models for engineering applications. *AIAA Journal*, 32:1598–1605.

[21]F.R. Menter. Improved two-equation k-omega turbulence models for aerodynamic flows. Technical report, 1992.

[22]F.R. Menter. Influence of freestream values on k-omega turbulence model predictions. *AIAA Journal*, 30(6), 1992.

[23]S. Candel. Numerical solution of conservation equations arising in linear wave theory: application to aeroacoustics. *Journal of Fluid Mechanics*, 83:466–493, 1977.

[24]G.M. Lilley. Fourth Monthly Progress Report on contract F-33615-71-C-1663. Appendix: generation of sound in a mixing region. Technical report, Lockheed Aircraft Company, Marietta, Ga., 1971.

[25]T. Colonius, S.K. Lele, and P. Moin. Sound generation in a mixing layer. *Journal of Fluid Mechanics*, 330:375–409, 1997.

[26]D.W. Wundrow and A. Khavaran. On the applicability of high-frequency approximations to Lilley's equation. *Journal of Sound and Vibration*, 272:793–830, 2004.

[27]C. Bailly, C. Bogey, and S. Candel. Modelling of sound generation by turbulent reacting flows. *International Journal of Aeroacoustics*, 9(4):461–490, 2010.

[28]M.S. Howe and J.E. Ffowcs Williams. On the noise generated by an imperfectly expanded supersonic jet. 1977.

[29]C.K.W. Tam and L. Auriault. Mean flow refraction effects on sound radiated from localized sources in a jet. *Journal of Fluid Mechanics*, 370:149–174, 1998.